ADVANCED
FUNCTIONAL
MATERIALS
www.afm-journal.de

Materials Views
www.MaterialsViews.com

FULL PAPER

Biosynthesis of Zinc Substituted Magnetite Nanoparticles with Enhanced Magnetic Properties

James M. Byrne,* Victoria S. Coker, Eva Cespedes, Paul L. Wincott, David J. Vaughan, Richard A. D. Pattrick, Gerrit van der Laan, Elke Arenholz, Floriana Tuna, Martin Bencsik, Jonathan R. Lloyd, and Neil D. Telling

The magnetic moments of magnetite nanoparticles are dramatically enhanced through the addition of zinc in a microbiologically driven synthesis procedure. The particles are produced through the reduction of Fe(III)-compounds containing Zn(II) by the iron reducing bacterium Geobacter sulfurreducens. Results indicate a significant increase in the saturation magnetization by over 50% compared to magnetite at both room and low temperatures for relatively minor quantities of zinc substitution. A maximum saturation magnetization of nearly 100 emu g^{-1} of sample is measured at room temperature. Analysis of the cation site ordering reveals a complex dependence on the Zn content, with the combined effect of Zn substitution of Fe^{3+} ions on tetrahedral sites, together with Fe^{2+} cation oxidation, leading to the observed magnetization enhancement for low Zn doping levels. The improved magnetic properties give superior performance in MRI applications with an MRI contrast enhancement among the largest values reported, being more than 5 times larger than a commercial contrast agent (Feridex) measured under identical conditions. The synthesis technique applied here involves an environmentally benign route and offers the potential to tune the magnetic properties of magnetic nanoparticles, with increased overall magnetization desirable for many different commercial applications.

1. Introduction

The synthesis of magnetic nanoparticles for use in a number of potential applications has been a focus of recent research. These applications include targeted cancer therapies, drug and gene delivery, MRI contrast agents, ferrofluids, magnetic recording materials, and bioremediation technologies.[1–4] Magnetic nanoparticles such as magnetite (Fe$_3$O$_4$) and transition metal-doped ferrites of the form M_xFe$_{3-x}$O$_4$ (M = Mn, Co, Ni, Zn, etc.) offer promising materials due to their intrinsic magnetism and small size, with manipulation of stoichiometry providing a method of tailoring the properties to specific applications.[5] In particular, the ability to increase the magnetic moment has great significance, for example in MRI imaging where it can enhance the effectiveness of magnetic contrast agents, or in hyperthermia cancer therapies, where an increase in magnetization at a given applied field maximizes the heating power achievable.

Stoichiometric magnetite (Fe$_3$O$_4$) is an inverse spinel with the cations Fe^{2+}[B]:Fe^{3+}(A):Fe^{3+}[B] in a ratio of 1:1:1, where (A) and [B] represent tetrahedral and octahedral sites, respectively. The magnetic exchange in magnetite is governed by a combination of antiferromagnetic superexchange (SE) and ferromagnetic double exchange (DE) interactions. There are three antiferromagnetic SE interactions between the Fe^{3+} ions on the (A) and [B] sites, mediated by the oxygen (O) ions which are denoted A-O-A, B-O-B,

Dr. J. M. Byrne, Dr. V. S. Coker, Dr. P. L. Wincott, Prof. D. J. Vaughan, Prof. R. A. D. Pattrick, Prof. G. van der Laan, Prof. J. R. Lloyd
School of Earth, Atmospheric and Environmental Sciences
Williamson Research Centre for Molecular Environmental Science, University of
Manchester, Manchester, M13 9PL, UK
E-mail: james.byrne@uni-tuebingen.de
Dr. J. M. Byrne
Department of Geosciences
University of Tuebingen
Center for Applied Geoscience Sigwartstrasse 10
72076, Tuebingen, Germany
Dr. E. Cespedes, Dr. N. D. Telling
Institute for Science & Technology in Medicine
Keele University
Stoke-on-Trent ST4 7QB, UK

Prof. G. van der Laan
Diamond Light Source
Didcot, Oxfordshire, OX11 0DE, UK
Dr. E. Arenholz
Advanced Light Source
Lawrence Berkeley National Laboratory
Berkeley, CA, 94720, USA
Dr. F. Tuna
School of Chemistry
University of Manchester
Manchester, M13 9PL, UK
Dr. M. Bencsik
College of Arts and Science
School of Science & Technology
Nottingham Trent University
Burton Street, Nottingham, NG1 4BU

Materials Views
www.MaterialsViews.com

ADVANCED
FUNCTIONAL
MATERIALS
www.afm-journal.de

FULL PAPER

Table 1. Structural and magnetic properties of zinc-doped magnetite nanoparticles. $\langle d \rangle$ is mean particle size, σ is dispersion index, M_s is saturation magnetization.

Sample	Starting material	EPMA Final	x	TEM		XRD	M_s [emu g^{-1}]	
	At% Zn	At% Zn		$\langle d \rangle$ [nm]	σ	$\langle d \rangle$ [nm]	5 K	300 K
Zn$_0$	0	0	0	16.1 ± 0.5	0.3	21.3 ± 2.9	72	64
Zn$_{0.16}$	5	5.2	0.16	13.9 ± 0.3	0.3	17.6 ± 1.1	112	97
Zn$_{0.42}$	15	14.1	0.42	10.5 ± 0.3	0.3	11.4 ± 2.9	112	72
Zn$_{0.56}$	20	18.6	0.56	10.5 ± 0.1	0.2	9.5 ± 1.2	102	56
Zn$_{0.92}$	33	30.6	0.92	8.3 ± 0.1	0.2	6.9 ± 1.1	40	12

and A-O-B. As pointed out by Néel,[6] in the simplest model, ferrimagnetism in Fe_3O_4 is obtained without any DE interaction, forcing an antiparallel alignment of the moments on the (A) and [B] sites. Since the antiparallel Fe^{3+}(A) and Fe^{3+}[B] moments compensate each other, a saturation magnetization of 4 μ_B/f.u. (formula unit) is expected from the remaining Fe^{2+}[B] moments. This simple Néel model has been extended by Yafet and Kittel,[7] who proposed a more elaborate model in which the B sublattice is subdivided into two (Fe^{2+} and Fe^{3+}) sublattices. It was shown that on weakening the A-O-B interaction and strengthening the B-O-B interaction, the B site magnetic moments are no longer rigidly parallel to the A site moments. The stronger B-O-B SE interaction results in spin canting, and thus a reduction in the saturation magnetization.

Based on the theory of this model and experimental evidence, the substitution of other metal cations within the structure of magnetite can be used to change the magnetic properties of nanoparticles in different ways, depending upon where the dopant is incorporated, for example, Ni^{2+} and Co^{2+} can substitute for Fe^{2+}[B], whereas Zn^{2+} has a strong affinity for the tetrahedral (A) site.[8,9] Of particular interest has been the substitution of Fe^{3+}(A) by diamagnetic Zn^{2+} which leads to a decrease in the magnetic component that is antiparallel to the Fe^{3+}[B] moment, hence would be expected to yield larger total magnetization which increases as zinc concentrations increase. This is seen to be the case only up to a certain percentage of zinc[10] because exchange interactions within the octahedral lattice begin to take over, resulting in spin canting.

A number of methods can be used for the synthesis of magnetic nanoparticles, including co-precipitation, hydrothermal approaches and mechanical ball milling, amongst others. These are often both economically and environmentally undesirable, due to the high temperatures and toxic chemicals used. Alternatively, biogenic approaches can also be used to produce magnetic nanoparticles in a method in which the anaerobic respiration of Fe(III) oxides by subsurface bacteria is utilized to produce magnetic nanoparticles. Fe(III) reducing bacteria are able to generate large amounts of extracellular magnetite at ambient temperature through the oxidation of an electron donor (organic matter or hydrogen), coupled with the reduction of metal cations such as Fe(III). Using this approach, Fe(III)-oxyhydroxides (and related phases containing other transition metals) can be reduced, producing soluble Fe^{2+} which re-crystallizes into a new mineral phase such as goethite, magnetite or siderite, depending upon the synthesis conditions (including pH, cell concentration, geochemical matrix and temperature).[11–13]

There have been many successful attempts to produce magnetic nanoparticles through the microbial reduction of Fe(III) oxides, including several which have demonstrated the ability to incorporate transition metal dopants into the crystal structure.[14–16] Most recently, the high temperature iron reducing bacterium *Thermoanaerobacter* TOR-39 (incubated at 65 °C) was used to produce zinc doped ferrite nanoparticles[17] which exhibited higher magnetic moments than stoichiometric magnetite nanoparticles. Additional benefits of using biological approaches to synthesizing magnetite nanoparticles over chemical methods include the functionalization of particle surface with organic matter. Ordinarily this is carried out in the post production stage, however the microbial interaction with the nanoparticles appears to yield a coating which is suited to sorption of catalysts such as palladium.[18] The ability to synthesize biogenic magnetite nanoparticles in large scale quantities has also been demonstrated,[15] thus validating the potential to be used as a commercial product.

The overall aim of this work is to generate nanoparticles with enhanced room temperature magnetic moments compared to those currently achievable by other means[19] through the microbial reduction of Fe(III) oxyhydroxides containing various concentrations of zinc at ambient temperatures by the iron reducing bacterium *Geobacter sulfurreducens*. The temperature of synthesis is thought to have a potential impact on the ordering of cations within the crystal structure[17] which would have a direct impact on overall magnetic moment of the nanoparticles. It is anticipated that the low temperature iron reduction in this work could ultimately lead to zinc ferrites with higher values of saturation magnetization than counterparts produced using high temperature synthesis.

2. Results and Discussion

2.1. Structural Properties

The ratios of zinc to iron in the substituted magnetite nanoparticles were determined by electron probe microanalysis (EPMA) and showed that a large proportion of the Zn was incorporated into the spinel structure. From the EPMA results, the values of x in the formula unit $Zn_xFe_{3-x}O_4$ were determined (**Table 1**).

The particles were imaged by transmission electron microscopy (TEM) (**Figure 1**) with the images showing mostly spherical particles, some sub-rounded particles and some with an indication of hexagonal facets. The size distribution of the
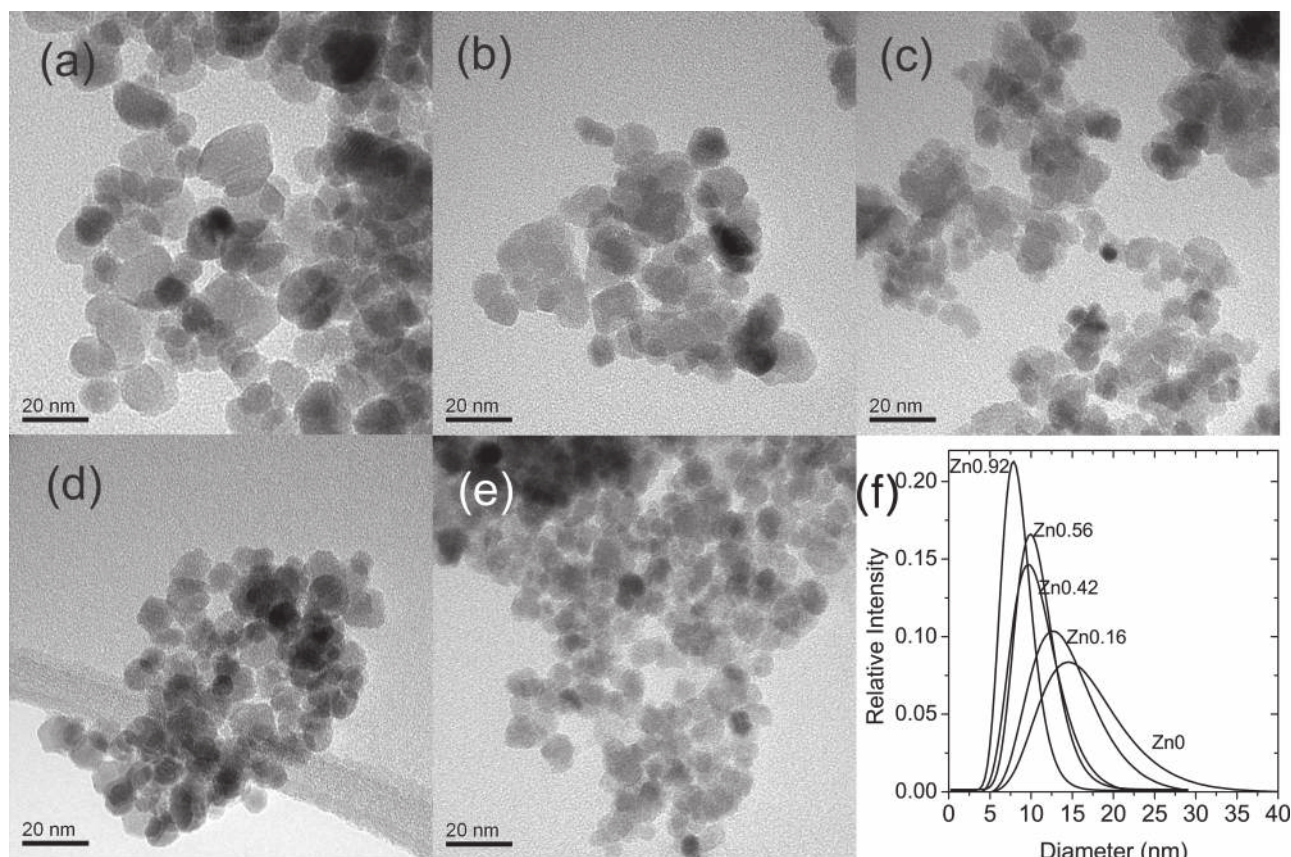
Figure 1. TEM images showing a) Zn_0, b) $Zn_{0.16}$, c) $Zn_{0.42}$, d) $Zn_{0.56}$, e) $Zn_{0.92}$, and f) size distributions of all samples obtained by measurement of $n = 200$ particle diameters per sample.

particles was determined by measurement of 200 particles per sample on TEM images, resulting in the distribution curves shown in Figure 1f. As more zinc entered the magnetite structure, the size range became narrower, with mean diameter decreasing. Samples $Zn_{0.42}$ and $Zn_{0.56}$ had very similar mean particle sizes and size distributions, and potentially provide the best comparisons between other properties such as magnetism and cation distributions, without particle size effects having to be taken into account explicitly. The absence of any major polydispersivity in the size distributions of the samples suggests that there is a high level of homogeneity within each of the samples and no significant amount of additional mineral phases. Energy dispersive X-ray (EDX) spectroscopy was used to confirm the relative ratio of Fe to Zn throughout the series. Zinc was measured to amount to 4.2%, 16.4%, 20.2%, and 34.0% of the total transition metal total for samples $Zn_{0.16}$, $Zn_{0.42}$, $Zn_{0.56}$, and $Zn_{0.92}$ respectively. These values match closely to those expected from the starting material, and the values measured using EPMA.

Powder X-ray diffraction (PXRD) data (**Figure 2**) confirmed the presence of magnetite in all samples, with siderite also detected in all samples, although this secondary phase was not observed using TEM. Siderite ($FeCO_3$) has previously been reported as an impurity in biogenically produced magnetite samples,[11] presumably formed via the interaction between

excess Fe^{2+} formed by the bacteria with carbonate in the buffer system used ($NaHCO_3$), Evidence of this mineral phase was not found using TEM, suggesting that it is a minor mineral phase that was successfully removed by the washing and magnetic separation procedures used prior to TEM analysis.

Crystallite particle size analysis was carried out using the most intense magnetite reflections (2 2 0), (3 1 1), (4 0 0), (5 1 1), and (4 4 0), with results indicating that an increase in the zinc concentration in the starting material led to the production of smaller crystallites, supporting the observations from the TEM images. Furthermore, there is no observable patterns visible which correspond to zincite (ZnO), thus suggesting that the zinc is present only in the magnetite crystal structure.

Values of the magnetite lattice constant (a_0) were determined for each sample by measuring positions of all main magnetite reflections and taking the average; these are plotted against zinc concentration (Figure 2c). The diffraction peaks showed an increase in the lattice constant a_0 for the magnetite nanoparticles from 8.37 Å to 8.45 Å as zinc concentrations increased, which is in close agreement with the findings of Tian et al.[20] Values of a_0 were determined for all samples through measuring positions of all main peaks, and with the averages plotted against zinc concentration (Figure 2c). The increase in a_0 with increasing zinc can be ascribed to the larger ionic radius of Zn^{2+} compared with Fe^{3+} in tetrahedral coordination (0.060 nm and

www.MaterialsViews.com

ADVANCED
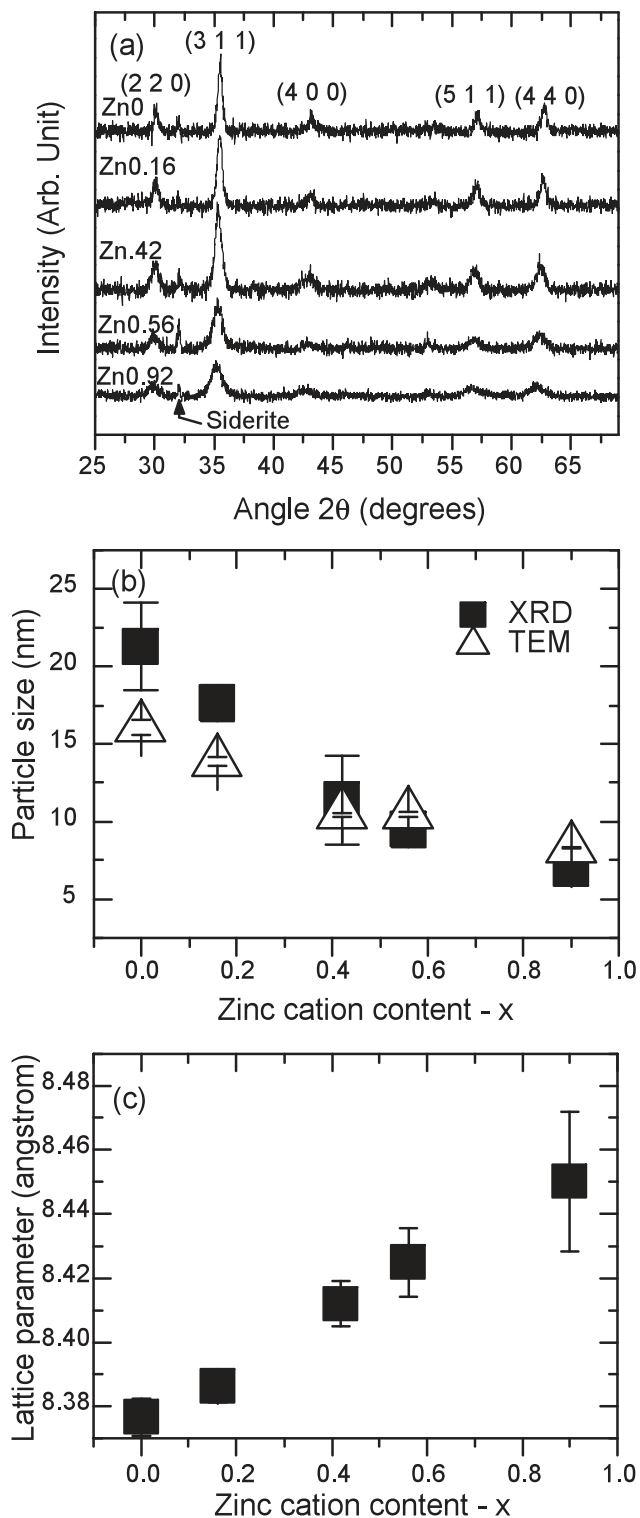FUNCTIONAL
MATERIALS
www.afm-journal.de

FULL PAPER

Figure 2. Powder X-ray diffraction data. a) XRD patterns displaying magnetite and zinc doped magnetite peaks. Siderite is also present. b) Mean crystallite particle size from powder XRD compared to TEM determined by fitting a Lorentzian curve to all peaks, then using the Scherrer equation to calculate mean particle size, compared against TEM determined mean size. c) Lattice parameter for magnetite with error bars determined from the standard deviation from the mean of all fitted powder XRD reflections.

0.049 nm, respectively).[21,22] This result shows that the incorporation of Zn^{2+} is not confined to the surface regions of the magnetite particles but involves the bulk structure.

2.2. Nanoparticle Magnetism

Changes in the magnetic properties of the particles were determined using superconduction quantum interface device (SQUID) magnetometry, including measurements of saturation magnetization (M_s), coercivity (H_c, the applied field required to reverse magnetization direction) and blocking temperature (T_B, the temperature above which a particle exhibits superparamagnetism). Hysteresis loops collected at room temperature (300 K) and at low temperature (5 K) between –6 T and +6 T (**Figure 3**a,b) show the maximum magnetization achievable in the nanoparticles in the presence of an applied magnetic field. The results show that as zinc is incorporated into the magnetite structure, M_s initially increases before decreasing again. At low temperatures, M_s (Table 1) for magnetite (Zn_0) was 72 emu g^{-1} and the M_s was seen to increase by 56% reaching a maximum of 112 emu g^{-1} for $Zn_{0.16}$ and $Zn_{0.42}$. M_s starts to decrease again at $Zn_{0.56}$, although with a value still higher than that of Zn_0, before reaching a minimum of 40 emu g^{-1} for $Zn_{0.92}$. The trend at room temperature differs slightly, with the maximum M_s reached at $Zn_{0.16}$ (97 emu g^{-1}) and decreasing for higher Zn concentration, with $Zn_{0.56}$ (56 emu g^{-1}) and $Zn_{0.92}$ (12 emu g^{-1}) samples having a smaller saturation magnetization than Zn_0.

It is expected that Zn^{2+} enters the tetrahedral site, and once there is a sufficient amount, it gives a weakening of the A-O-B interaction as described by the Yafet and Kittel model.[6] The B-O-B interaction then begins to dominate leading to spin canting which reduces the saturation magnetization as seen in the SQUID measurements. Enhanced M_s in biogenic zinc doped ferrites compared to biogenic magnetite has previously been reported by Love et al., although with a more modest enhancement 29%[23] (measured at 5 K), compared to 56% in this study for $Zn_{0.16}$. However, of particular significance is that a much less dramatic temperature dependence of the magnetization is observed here than in previous studies.[23–26] This yields remarkably high magnetic moments in the nanoparticles even at room temperature. The values observed are comparable with $Zn_xFe_{3-x}O_4$ nanoparticles prepared by Jang et al. In that study a series of particles were produced with consistent diameters of 15 nm[27] and achieved a maximum room temperature M_s of 99.3 emu g^{-1} for $x = 0.4$ (where the value of M_s is adjusted here from emu g^{-1} magnetic atom to emu g^{-1} $Zn_xFe_{3-x}O_4$ for direct comparison). The ability to maintain constant particle size explains why these authors observe an increase in M_s for Zn doping up to $x = 0.4$.

Although PXRD measurements showed the presence of siderite, there should be no influence on the hysteresis loops from this antiferromagnetic[28] material, given the low proportion present in the samples. Additionally, it is important to note that M_s is dependent upon the crystallite size of a material, with larger particles exhibiting higher M_s than smaller particles.[29] Based upon the observations seen in Figures 1, 2 that the average size of the zinc-doped nanoparticles decreases with zinc concentration, the changes in saturation magnetization
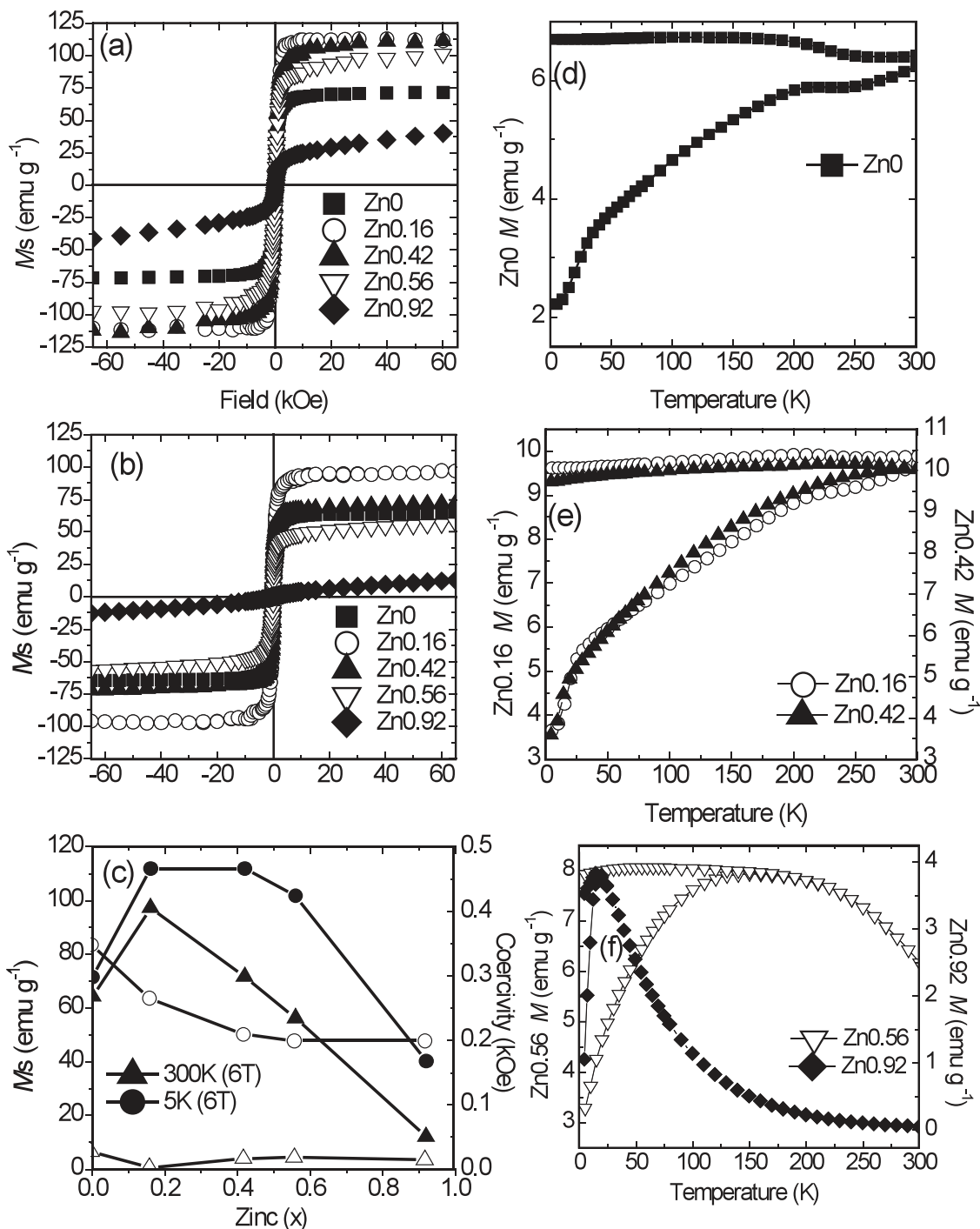
Figure 3. SQUID magnetometry. a) 5 K hysteresis loops, b) 300 K hysteresis loops, c) variations in saturation magnetization M_s, and coercivity H_c obtained from hysteresis loops. d–f) FC and ZFC curves highlighting changes in magnetization of nanoparticles as a function of temperature.

shown in Figure 3c, although dramatic, are actually below the optimum values that could theoretically be achieved if the samples had the same mean diameter. The reason for the decrease in particle size with increasing zinc content is not clear from the results presented however it is an effect that we have also observed with the incorporation of Co as a dopant in biogenic magnetite[5]. In that study, the decrease in particle size

with increasing dopant concentration was considered to be due to several different factors including the rate of microbial Fe(III)-reduction, the potential heavy metal toxicity to the bacteria and the total number of Co-ferrihydrite particles present in the experiments which could act as nucleation sites. Whilst it is not known which factor plays the dominant role in these experiments, we have shown previously that the size of

Materials
Views
www.MaterialsViews.com

ADVANCED
FUNCTIONAL
MATERIALS
www.afm-journal.de

FULL PAPER

magnetite nanoparticles produced via Fe(III)-reduction by *G. sulfurreducens* can be controlled by changing the amount of bacteria introduced at the start of the experiment[11]. By applying this approach it should therefore be possible to produce larger nanoparticles which could potentially exhibit even larger M_s values than those reported here.

The superparamagnetic transition was also studied by measuring field cooled (FC) and zero-field cooled curves (ZFC). The spectra show that the blocking temperature T_B, of Zn_0 and $Zn_{0.16}$ must be above room temperature, because the ZFC and FC curves

do not intersect at any point, unlike those for $Zn_{0.42}$ where a T_B of ≈270 K can be deduced (Figure 3d,e). Similarly, the maxima observed in Figure 3f for $Zn_{0.56}$ (≈170 K) and $Zn_{0.92}$ (≈20 K) correspond to the blocking temperatures (T_B) of those samples.

2.3. Cation Distributions

Figure 4a,b show the X-ray absorption spectra (XAS) at the Fe $L_{2,3}$ and Zn L_3 edges, respectively, with the maximum of the
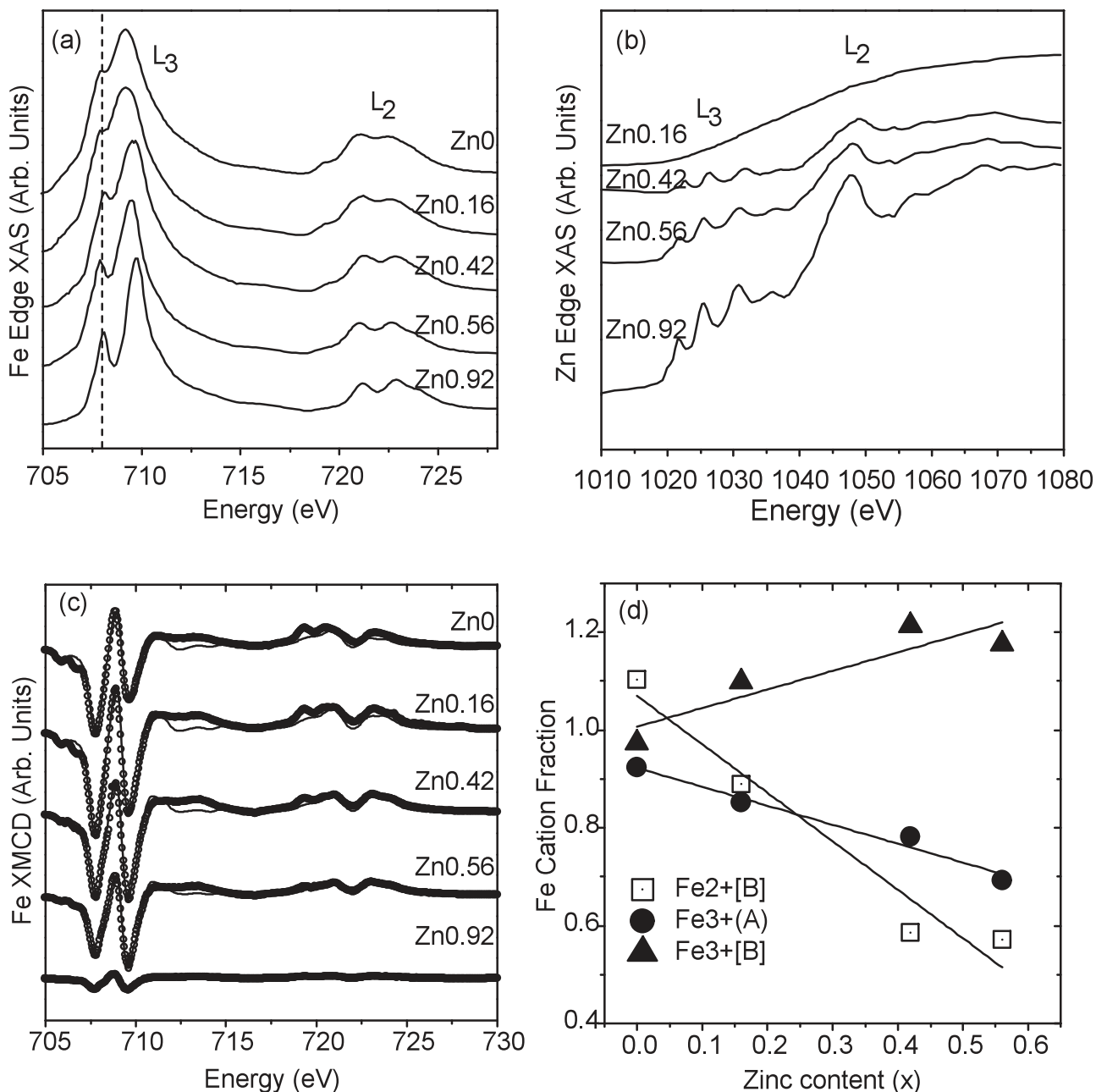

Figure 4. X-ray absorption data. a) XAS of Fe $L_{2,3}$ edge, shoulder feature on low energy side of Fe L_3 edge indicates increase in B site Fe^{3+}, b) XAS of Zn $L_{2,3}$ edge, c) XMCD of Fe $L_{2,3}$ edge measured at room temperature. Solid line corresponds to the fit of the data points for each sample. d) cation distributions determined through fitting of Fe XMCD spectra.

Table 2. XMCD fitting results with cation values accurate to ±0.02.

Sample	Iron cation occupancies				Octahedral and Tetrahedral site ratios			
	$Fe^{2+}[B]$	$Fe^{3+}(A)$	$Fe^{3+}[B]$	Zn^{2+}	Fe(A)%	Fe[B]%	$Zn^{2+}(A)$	$Zn^{2+}[B]$
Zn_0	1.1	0.92	0.97	0	30.8	69.2	0.00	0.00
$Zn_{0.16}$	0.89	0.85	1.1	0.16	30	70	0.13	0.03
$Zn_{0.42}$	0.59	0.78	1.21	0.42	30.3	69.7	0.22	0.21
$Zn_{0.56}$	0.57	0.69	1.18	0.56	28.4	71.6	0.25	0.32
$Zn_{0.92}$	0.38	0.7	1.03	0.92	33.2	66.8	0.17	0.76

average Fe spectra normalized to one. It is clear from the Fe L edge spectra that, as the zinc concentration increases through the series, the shoulder feature on the low energy side of the L_3 edge becomes increasingly resolved into a separate peak. Such a feature is normally observed in oxidized magnetite samples, and reveals a decrease in the Fe^{2+} concentration in the magnetite relative to the Fe^{3+} concentration. The Zn L_3 edges of the doped nanoparticles display spectra corresponding to those reported for a bulk $ZnFe_2O_4$ powder,[30] thus showing incorporation of the Zn into the iron oxide spinel rather than formation of additional particles at the surface, in agreement with XRD lattice constant measurements. The intensity of the Zn L_3 spectra increases with zinc concentration as expected.

X-ray magnetic circular dichroism (XMCD) data for the Zn doped samples are presented in Figure 4c. The intensity of the XMCD spectrum is a measure of the magnetization of the particles, provided that the average of the two associated XAS spectra has been normalized to one. This is demonstrated by sample $Zn_{0.16}$ appearing to be more magnetic than Zn_0 with $Zn_{0.92}$ exhibiting only a very small magnetic component. The peaks in the Fe L_3 edge XMCD correspond to the relative amounts of ferrous and ferric iron oxidation states and their coordination environment, with $Fe^{2+}[B]$ matching the first negative peak (lowest energy), $Fe^{3+}(A)$ the positive peak and $Fe^{3+}[B]$ the second negative peak. The spectra show that, as initial zinc concentration increases, there is both a decrease in the intensity of the peaks associated with octahedral site Fe^{2+} and tetrahedral site Fe^{3+}, and an increase in octahedral site Fe^{3+}. Fitting of the data using calculated spectra confirms this interpretation (see **Table 2** and Figure 4d).

Stoichiometric magnetite has a total electronic charge of zero, with the positive charges on the iron offset by the negative charge on the oxygen, that is, one Fe^{2+} and two Fe^{3+} ions are neutralized by four O^{2-} ions. If Zn^{2+} displaces tetrahedral Fe^{3+} as observed, a charge imbalance is created. However, for overall charge neutrality to be maintained, for every Fe^{3+} ion displaced by Zn^{2+}, one Fe^{2+} ion would need to oxidize to Fe^{3+}. Figure 4d illustrates the changes in Fe cation site occupancies with respect to zinc substitution as determined by fitting XMCD spectra measurements. The decrease in Fe^{3+} tetrahedral mirrors the increase in Fe^{3+} octahedral site occupancies as zinc increases, as would be expected if one unit of $Fe^{2+}[B]$ was oxidized to $Fe^{3+}[B]$ in order to balance the overall charge when $Fe^{3+}(A)$ is replaced by $Zn^{2+}(A)$.

An unexpected observation is the significantly faster decrease in $Fe^{2+}[B]$ than $Fe^{3+}(A)$ as Zn is added, as shown by

the more negative gradient of the straight line fit for $Fe^{2+}[B]$ sites compared to $Fe^{3+}(A)$ sites (Figure 4d). If Zn^{2+} was only entering $Fe^{3+}(A)$, the decrease in $Fe^{2+}[B]$ should exactly compensate the decrease in $Fe^{3+}(A)$ in accordance with the formula, $[Zn^{2+}_x Fe^{3+}_{1-x}](Fe^{2+}_{1-x}Fe^{3+}_{1+x})O_4$.[31] The result suggests that there is also substitution of Zn^{2+} into the octahedral sites in place of $Fe^{2+}[B]$. Previous work using various techniques, including neutron scattering and muon spin rotation/relaxation, shows that zinc has very strong affinity for the tetrahedral sites in the spinel,[32,33] hence stoichiometric zinc ferrite is expected to be an normal spinel $(Zn^{2+})_A[Fe^{3+}_2]_BO_4$. However, the partial inversion of zinc ferrite has been observed previously in studies of nanoscale materials (<50 nm)[30,34] and this appears to agree with the results of the present study. The substitution of Zn^{2+} into the octahedral site in place of Fe^{2+} would not affect the overall charge balance of the nanoparticles, hence its incorporation would not affect either of the Fe^{3+} cations. From the fitting results of $Fe^{2+}[B]$, $Fe^{3+}(A)$ and $Fe^{3+}[B]$ (Table 2), it is possible to estimate the relative occupancy of zinc in both tetrahedral and octahedral coordination by representing the formula for zinc ferrite as $[Zn^{2+}_y Fe^{3+}_{1-y}]_A(Zn^{2+}_{x-y}Fe^{2+}_{1-x}Fe^{3+}_{1-y})_BO_4$, where y is the total (A) site zinc, and x is the total zinc. Using the occupancies of each iron cation, values of $Zn^{2+}(A)$ and $Zn^{2+}[B]$ were determined (Table 2). The results show that for low Zn_x samples, whilst there is some incorporation of zinc into [B] sites, the preference for incorporation is on the (A) site. The values obtained for $Zn_{0.42}$ show $Zn^{2+}(A)$ and $Zn^{2+}[B]$ to be roughly equal, however, as there are twice as many B sites than A sites in the spinel, the preference can still be thought to remain with tetrahedral substitution. It is only in sample $Zn_{0.92}$, where $Zn^{2+}[B]$ is more than double $Zn^{2+}(A)$ that one can say the zinc is now preferentially incorporated into an octahedral environment. Interestingly, none of the cases is close to a random distribution of Zn, which would give the formula $[Zn^{2+}_{x/3}Fe^{3+}_{1-x/3}]_A(Zn^{2+}_{2x/3}Fe^{2+}_{1-x}Fe^{3+}_{1+x/3})_BO_4$ which highlights the superior ordering of substituted cations using biogenic nanoparticle production.

The reason for this change in zinc substitution preference is not known; it could be an effect of particle size (i.e., the larger surface area gives a preference for one particular site). A similar result was reported by Ehrhardt et al. for $ZnFe_2O_4$ where the amount of [B] site zinc increased over (A) site with decreasing particle size.[35] However, the occupancy changes could also be attributed to the changing value of zinc content (x), with additional Zn weakening the exchange interactions and changing the partitioning, or even to the new biological

www.MaterialsViews.com

ADVANCED
FUNCTIONAL
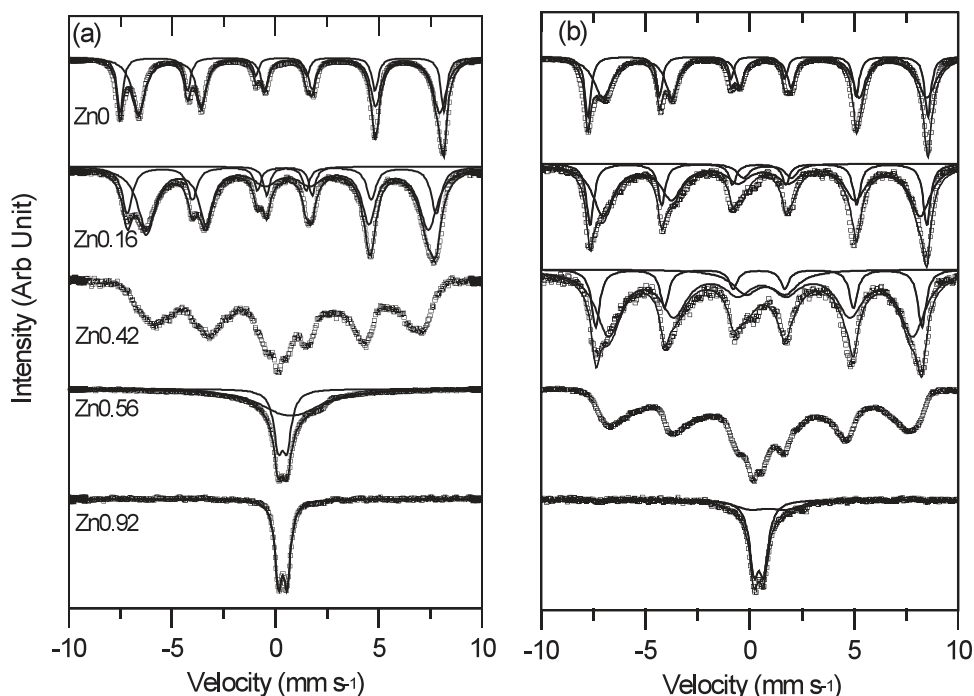MATERIALS
www.afm-journal.de

FULL PAPER

Figure 5. Mössbauer spectra collected for five zinc doped samples. Solid lines correspond to the fits to the data points. a) Room temperature measurements shows clear hyperfine structure for sample Zn_0 and $Zn_{0.16}$ and a transition between the superparamagnetic and ferrimagnetic state for $Zn_{0.42}$. b) Low temperature measurements at 110 K show some hyperfine field structure for all samples except $Zn_{0.92}$.

methods by which the particles were produced which take place at low temperatures and may affect cation ordering.[17] Further investigation is required to determine the reason behind the inversion of Zn occupancy.

Mössbauer spectra (^{57}Fe) were collected for all five zinc ferrite samples (**Figure 5**) at room temperature (300 K) and low temperature (≈110 K). Parameters including isomer shift (IS), quadrupole splitting (ΔE_Q) and hyperfine field (B_{hf}) were obtained through fitting of the spectra (**Table 3**). Sample Zn_0, shows spectra characteristic of magnetite with two Zeeman patterns visible due to ferric ions in tetrahedral sites, and ferrous and ferric ions in the octahedral environment.[36] As zinc incorporation increases, the hyperfine field pattern collapses (samples beyond $Zn_{0.42}$ at 300 K and beyond $Zn_{0.56}$ at 110 K) until the spectra display only a doublet pattern for $Zn_{0.92}$. These changes parallel the results obtained from SQUID ZFC/FC curve analysis which show that the blocking temperatures are below room temperature for $Zn_{0.42}$, $Zn_{0.56}$ and $Zn_{0.92}$. The T_B of $Zn_{0.42}$ is ≈270 K as measured by SQUID; however, this sample exhibits a range of sizes and some particles will not be entirely blocked, even at 300 K. This gives rise to a mixture of hyperfine field sextet and paramagnetic doublet spectra as observed. The same applies to $Zn_{0.56}$ which also shows Zeeman splitting and doublets present in measurements at 110 K.

Samples $Zn_{0.16}$ (300 K and 110 K) and $Zn_{0.42}$ (110 K) consist of sharp Lorentzian lines corresponding to the two overlapping sextets as observed for Zn_0 (Figure 5). The line shape of the [B] site sextet is quite broad suggesting that the octahedral component is made up of several overlapping sextets. Fitting of

the individual spectra was not possible; however, such sextets have previously been suggested and are attributed to nearest neighbor interactions.[37] At high zinc content ($Zn_{0.56}$) a significant number of octahedral cations have insufficient nearest neighbor magnetic Fe^{3+}(A) cations to have ordered spins, giving rise to a quadrupole split doublet and an incomplete hyperfine field even well below the material's blocking temperature (170 K). Sample $Zn_{0.92}$ exhibits only quadrupole split patterns because there are insufficient nearest neighbor exchange interactions between ferric and ferrous cations, despite the presence of some Fe^{2+} in the octahedral environment as observed by XMCD.

Fitting of Zn_0 (biogenic magnetite) shows the sample to have isomer shifts and hyperfine fields for (A) and [B], which match very closely with those commonly observed for magnetite at room temperature.[38–40] The $Zn_{0.16}$ LT and RT, and $Zn_{0.42}$ LT spectra cannot be accurately fitted without the addition of a doublet with parameters most accurately match those of an Fe^{2+} mineral[40] and is most likely due to the carbonate mineral siderite which was observed in PXRD measurements. The general trend in IS shown by the first three spectra (Table 3) indicate that, as the zinc concentration increases, the [B] site IS decreases as would be expected if Fe^{2+}[B] was replaced with Fe^{3+}[B] to maintain charge neutrality. IS values of the (A) site remain relatively unchanged, indicating that there is no reduction of Fe^{3+}(A) to Fe^{2+}(A), or incorporation of Fe^{2+}(A) during the formation of the magnetic nanoparticles. The B_{hf} of both sites decrease with increasing zinc content (Zn_0 to $Zn_{0.42}$ inclusive). This is thought to be due to a decrease in exchange interaction

Table 3. Extracted Mössbauer parameters. IS is isomer shift, ΔE_Q is quadrupole splitting, B_{hf} is hyperfine field, (A) is tetrahedral site sextet, [B] is octahedral site sextet, and Db is doublet.

Sample	Temperature K	Site	IS [mm s^{-1}]	ΔE_Q [mm s^{-1}]	B_{hf} (kOe)	Population [%]
Zn$_0$	300	(A)	0.30	0.02	486.0	33.0
		[B]	0.65	0.02	451.6	67.0
	110	(A)	0.39	0.00	505.7	33.3
		[B]	0.74	−0.01	482.2	66.7
Zn$_{0.16}$	300	Db	0.68	2.20	–	5.5
		(A)	0.31	0.00	463.7	28.0
		[B]	0.58	0.00	422.8	66.6
	110	Db	0.85	2.31	–	5.4
		(A)	0.44	−0.02	501.0	28.0
		[B]	0.61	−0.04	471.6	66.6
Zn$_{0.42}$	300	–	–	–	–	–
	110	Db	0.76	1.90		12.1
		(A)	0.44	0.00	485.4	19.8
		[B]	0.56	−0.03	452.2	68.1
Zn$_{0.56}$	300	Db1	0.35	0.42	–	38.5
		Db2	0.75	1.06	–	61.5
	110	–	–	–	–	–
Zn$_{0.92}$	300	Db1	0.36	0.41	–	100.0
	110	Db1	0.44	0.46	–	68.0
		Db2	0.88	1.69	–	32.0

between (A) and [B] sublattices as the total number of nearest-neighbor magnetic interactions (A-O-B) decreases as zinc is substituted into the magnetite crystal lattice.

The doublet parameters for Zn$_{0.92}$ closely match values previously observed for stoichiometric zinc ferrite ZnFe$_2$O$_4$[41–43] (albeit with a slightly larger quadrupole splitting). The increased quadrupole splitting has been observed previously at room temperature by Ehrhardt et al.[35] whilst studying size-dependent effects in nanosized ZnFe$_2$O$_4$ with smaller particle size leading to increasing ΔE_Q. In that study, the increase was attributed to the zinc substitution preference switching from (A) to [B] sites as particle size decreases. This inversion of site preference was observed here using XMCD, but the results from both techniques are unable to determine any conclusive reason for Zn being incorporated into the octahedral sites. The emergence of a second doublet in Zn$_{0.92}$ at low temperature points to the possible formation of a Zeeman pattern, as temperature decreases and the sample becomes magnetically ordered as observed in previous studies on zinc ferrite.[44,45]

2.4. Application to Magnetic Resonance Imaging

The significance of the reported enhancement of the magnetic moment by Zn doping for MRI biomedical application is shown here. The ability of magnetic contrast agents to increase the rate of nuclear magnetic resonance (NMR) relaxation of surrounding protons is mostly based on their effect on the spin–spin T_2 relaxation parameter. T_2 contrast reflects the ability of the nanoparticles to produce local magnetic inhomogeneities in the applied magnetic field and therefore, the MRI contrast enhancement effects are directly related to the magnetization of the nanoparticles. The contrast efficiency is given by the relaxivity (r_2), being the slope of R_2 (or $1/T_2$) plot as a function of the nanoparticles concentration. To evaluate MRI efficiency in this study, agar phantoms were prepared from stable water-based nanoparticles suspensions obtained by a citric acid coating route.

MRI investigations were performed for samples Zn$_0$, Zn$_{0.16}$, and Zn$_{0.42}$ for different iron concentrations, ranging from 0.05 µg mL^{-1} to 2.5 µg mL^{-1}, at a polarizing field of 2.35 T (**Figure 6**). For comparison purposes, a standard MRI commercial contrast agent comprising conventional iron oxide nanoparticles, Feridex, was also measured under identical experimental conditions. R_2 results in Figure 6, show a linear dependence with iron content, and evidence enhanced transverse relaxivity of the biogenic Zn-doped ferrites in comparison with the commercial contrast agent. The highest relaxivity is obtained for Zn$_{0.16}$, showing a superior MRI contrast enhancement, being 5.2 times larger than Feridex (an increase of 415%), with Zn$_{0.42}$ being 4.5 times larger (an increase of 345%).

Comparing to literature, C. Bárcena et al. [24] have reported an increase of 91% (which is less than 1/4 times the enhancement here) in r_2 relaxivity over Feridex using mixed spinel hydrophobic ZnxFe$_{3-x}$O$_4$ nanoparticles encapsulated in polymeric micelles. Whilst, Jang et al. [27] have found critical

www.MaterialsViews.com

ADVANCED
FUNCTIONAL
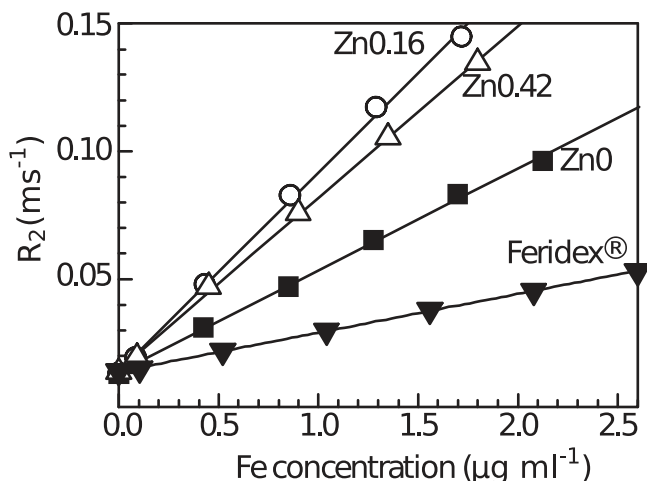MATERIALS
www.afm-journal.de

FULL PAPER

Figure 6. Proton transverse relaxation rate (R_2) versus the iron content for samples Zn_0 (■), $Zn_{0.16}$ (O), and $Zn_{0.42}$ (△) in comparison with a standard MRI contrast agent (Feridex) (O). Solid line corresponds to the linear fit of the data points for each sample.

enhancements of MRI contrast for 15 nm sized single crystalline and size monodisperse ($\sigma < 5\%$) Zn^{2+} doped synthetic nanoparticles of $Zn_xMn_{1-x}Fe_2O_4$ and $Zn_xFe_{1-x}Fe_2O_4$. This latter study found that $(Zn_{0.4}Fe_{0.6})Fe_2O_4$ and $(Zn_{0.4}Mn_{0.6})Fe_2O_4$ nanoparticles have MRI contrast effects that are 2.5 and 2 times larger than those of undoped Fe_3O_4 and $MnFe_2O_4$ nanoparticles, respectively. Similarly, we have obtained here a contrast effect 2 times larger than the undoped Fe_3O_4 using a biogenic route. Recent reviews of MRI contrast agents [46,47] show that doped-ferrite nanoparticles, such as $Zn_xFe_{1-x}Fe_2O_4$, $Mn_xFe_{1-x}Fe_2O_4$, and Fe core/ferrite shell of $Mn_xFe_{1-x}Fe_2O_4$ exhibit the highest R_2 among reported values (3 to 10 times Feridex). Although strict comparison between published data requires identical values of polarizing field, echo time, number of spin echoes and suspending medium self-diffusion coefficient, we notice that the largest relaxivity obtained here (5.2 times Feridex for $Zn_{0.16}$) remains among the largest reported enhancements.

Furthermore, the expected key effect of the enhanced magnetic response of the nanoparticles on their MRI performance is evidenced here: the relaxivity properties vary according to the trend of the saturation magnetization of the nanoparticles at room temperature, with the largest contrast enhancement corresponding to the maximum M_s reached at $Zn_{0.16}$ (97 emu g⁻¹). This clearly demonstrates the fundamental role of the intrinsic magnetic properties for the biomedical performance of the nanoparticles.

3. Conclusions

In this work, zinc has been incorporated into the crystal structure of magnetite to enhance the magnetic moment of magnetic nanoparticles. A range of zinc-doped magnetic nanoparticles containing varying concentrations of zinc were produced using biogenic reduction of Fe(III)-Zn(II) bearing minerals by the bacterium *Geobacter sulfurreducens*. An increase of 56% and 52% in the saturation magnetization of the particles (at 5 K and 300 K,

respectively) was achieved through a loading of only 5% zinc. Lattice parameter changes were determined through PXRD analysis, confirming that the zinc was incorporated into the crystal structure of the magnetite rather than forming a surface layer.

Changes in the cation distribution of iron and zinc within the crystal structure were investigated using XMCD and Mössbauer spectroscopy to further understand the interactions which dictate the magnetic properties. The results indicate the substitution of Fe^{3+}(A) sites with Zn^{2+}, combined with the oxidation of Fe^{2+}[B] sites to Fe^{3+}[B]. Additionally, evidence suggests that some zinc may have also entered into the octahedral sites in place of Fe^{2+}[B]. This effect is observed to increase throughout the series with Zn^{2+} being preferentially incorporated into the [B] site rather than (A) for the highest concentration zinc sample ($Zn_{0.92}$). It is thought that the "non-normal" cation ordering may be due to a combination of the size of the material, and the temperature at which it was produced. The location of iron within the lattice has a profound impact on the magnetic properties of the material, with the combined effect of substitution and reduction leading to a decrease in the antiparallel magnetic moments of the Fe^{3+} cations, plus an increase in the total Fe^{3+} present in [B] with respect to Fe^{2+} which have magnetic moments of 5 μ_B and 4 μ_B, respectively. These factors lead to the increase in M_s that is observable for the low zinc concentration samples in the series.

The decrease in overall magnetization as zinc continues to be incorporated is explained by exchange interactions between the crystal lattice sites. In stoichiometric magnetite, the A-O-B site interactions, mediated via oxygen atoms, dominate so as to align the A and B sites antiparallel. As Fe^{3+}(A) is replaced with diamagnetic Zn^{2+}, B-O-B site interactions begin to take over, initially resulting in spin canting, before aligning anti-parallel magnetic spins within the B site itself, hence the overall magnetic moment decreases and tends towards zero. In normal spinel Zn ferrite, antiferromagnetic superexchange interactions occur between Fe^{3+} ions located in B sites, whereas in a mixed spinel, the interactions occur between Fe^{3+} located in A and B sites.[48]

The key effect of the enhanced magnetic response of the nanoparticles on their MRI performance is demonstrated, with the relaxivity properties varying according to the evolution of the saturation magnetization of the nanoparticles at room temperature. Superior MRI performance of these biogenic Zn-doped samples is shown, leading to an MRI contrast enhancement among the largest reported ones, more than 5 times larger than a standard contrast agent (Feridex), for the sample showing the maximum saturation magnetization (nearly 100 emu g⁻¹) with only 5% of zinc loading.

To conclude, the precise control over the Zn cation substitution is required to reveal enhanced M_s. These results presented here demonstrate the significant potential of an environmentally benign biogenic route that could be used to achieve the desired level of control, leading to the production of high moment nanoparticles.

4. Experimental Section

Synthesis of Zinc–Iron Oxyhydroxides: Zn(II)–Fe(III) zinc–iron oxyhydroxides were synthesized by dissolving varying quantities of $ZnCl_2$ and $FeCl_3$ in aqueous solution, with the amount of $ZnCl_2$ added to each

sample designed to produce a molar ratio of 0, 5, 15, 20, and 33% Zn to Fe, respectively. Precipitation of a solid metal cation oxyhydroxide (MCO) was then facilitated through hydrolysis by 10 N sodium hydroxide, which was added until the final solution had a pH of 7.0. Chloride ions that were still present in solution were removed to prevent interference with microbial action by centrifugation of the MCO solution at 17000 g for 20 min with the supernatant being removed and the MCO re-suspended in deionised water. This process was repeated six times to ensure total removal of chloride ions. Total iron concentration was determined by the ferrozine assay.[49]

Bacterial Cultures: Starting microbial cultures were prepared in 500 ml bottles containing 50 mmol L^{-1} electron acceptor (MCO), 20 mm electron donor (sodium acetate), 30 mm buffer (sodium bicarbonate), and 10 μm of an electron shuttle (anthraquinone 2,6-disulphonate) to accelerate Fe(III) reduction. Cultures were prepared under a gas flow of $N_2:CO_2$ (80:20) and then separated into 100 mL bottles in an anaerobic cabinet, to maintain anoxic conditions. Sterility was ensured by autoclaving the bottles at 121 °C for 20 min. *Geobacter sulfurreducens* was grown at 30 °C under anaerobic conditions on modified freshwater medium[50] containing 25 mm sodium acetate and 40 mm sodium fumarate as the electron donor and acceptor respectively. After 24 h of growth, the late-log phase bacterial cultures were harvested by centrifugation at 5000g for 20 min, and washed twice in bicarbonate buffer (30 mm; pH 7). Following the final wash, the cell pellet was resuspended as a slurry with the optical density measured at 600 nm using an M501 single beam scanning UV/visible spectrophotometer. The Zn(II)-Fe(III) oxyhydroxide cultures were then inoculated with *G. sulfurreducens* (≈0.2 mg mL^{-1} protein) and incubated in the dark at 30 °C.

Nanoparticle Characterization: X-ray absorption spectroscopy (XAS) data at the Fe $L_{2,3}$ and Zn $L_{2,3}$ edges were acquired at the Advanced Light Source (ALS), Lawrence Berkeley National Laboratory, Berkeley, California, USA. XAS were collected in total-electron-yield (TEY) mode, using circularly polarized X-rays with the sample in an applied magnetic field of –0.6 T and +0.6 T, that is, parallel and antiparallel, respectively, to the direction of the beam. TEY mode has an effective probing depth of ≈3–4 nm, with the intensity exponentially falling off with depth. X-ray magnetic circular dichroism (XMCD) data were obtained using the difference between the two XAS spectra collected in opposite applied magnetic fields. XMCD spectra reveal changes in magnetization, site location and valence state (i.e., number of *d* electrons) and, for metal oxides, are able to provide information about magnetic cations with different oxidation states at different lattice sites[8,51]. Atomic multiplet calculations were applied to determine site distributions of Fe cations within the structure of the crystalline material[52,53]. The diamagnetism of Zn gives a zero XMCD signal. Dried samples were placed on carbon tape mounted onto a copper sample probe. Sample loading took place in an anoxic glove bag, with the sample probe encased in an airtight container to allow for transportation between glove bag and sample chamber. The container was removed as late as possible in a backflow of nitrogen to ensure as little exposure to air as possible and to maintain the oxidation state of the iron at the surface of the particles.

Mössbauer spectra were recorded with a FAST ComTek 1024-multichannel analyzer system using a constant acceleration drive (RT, γ-ray source ≈25 mCi ^{57}Co/Rh matrix). Measurements at low temperatures were carried out using a liquid nitrogen cryostat. For line fitting, the Lagarec/Rancourt Recoil fitting routine was utilised (Intelligent Scientific Applications Inc.). Spectra were fitted using Lorentzian line shape symmetrical doublets/sextets. Isomer shift data were calibrated with reference to Fe foil spectra recorded at RT. The absorber thickness was <4 mg Fe cm^{-2}.

Mineral phases were obtained using powder X-ray diffraction (PXRD) carried out using a Bruker D8 Advance instrument with Cu $K_{\alpha 1}$ source. Data were acquired over a 2θ range of 5–70° with, step size 0.02°. The average crystallite particle size of the magnetite was determined using the Scherrer equation by fitting a Lorentzian function to the (220), (311), (400), (511), and (440) reflections [54,55], with errors generated as the standard deviation from the mean.

Transmission electron microscopy (TEM) was carried out using a Philips CM 200 electron microscope at the Leeds Electron Microscopy and Spectroscopy (LEMAS) Centre, University of Leeds, UK. The microscope was equipped with a field emission gun, EDX detector (Oxford Instruments, ISIS software) and Gatan imaging filter (GIF200). All images were obtained using an operating beam voltage of 200 kV. Particle size distributions were determined by measurement of the diameter of a population size of n = 200 particles per sample.

Superconducting quantum interface device (SQUID) magnetometry was used to determine the magnetic properties of samples which were washed three times in deionised water and dried in a glovebox before being constrained in eicosane. Measurements were performed using a Quantum Design MPMS-XL SQUID equipped with a 7 T magnet, with zero-field cooled (ZFC) and field-cooled (FC) magnetization curves recorded between 5 K and 300 K in an applied magnetic field of 100 Oe. Residual diamagnetic signals detected from the sample holder and eicosane were measured and subtracted from the raw data. Saturation magnetization (M_S) values were determined as the maximum recorded magnetization and measured in emu g^{-1} of the whole sample.

The chemical composition of solid particles was determined using electron probe microanalysis (EPMA) with a Cameca SX100 microprobe equipped with wavelength dispersive spectrometer and operating at a voltage of 15 kV with a specimen current of 20 mA. Pure metals were used as standards.

Water-based nanoparticles suspensions were prepared by coating with citric acid (CA), as described elsewhere,[56] by conferring negative surface charge to the nanoparticles. Stability of the citric acid coated nanoparticles in water was confirmed by zeta potential measurements, obtaining values between –30 mV and –50 mV, what confirms good stability of the negatively charged suspensions. From the water suspensions, phantoms of 1.5% w/v agar have been prepared for MRI experiments.

Determination of the Fe content in the nanoparticles suspensions used for MRI investigations was done by Inductively Coupled Plasma (ICP) analysis, by digesting samples in high-purity nitric acid. Nanoparticles suspensions were mixed with concentrated nitric acid (70%) and heated at 60 °C for 48 h. Resulting samples were diluted with deionized water (up to final 2% nitric acid) and 0.2 μm filtered. Complete digestion of unfiltered highly concentrated nanoparticles suspension was previously confirmed by Dynamic Light Scattering measurements before and after digestion.

All MRI measurements were done at B_0 = 2.35 T with the Bruker Biospec MSME sequence, echo time T_E = 10.25 ms, 128 spin echoes, repetition time T_R = 4.5 s. Seven 2 mL Eppendorf vials were imaged simultaneously to obtain the data for seven different values of concentration. Relaxation values were further extracted with mono exponential fitting using MATLAB home built software applied on the raw echo images.

Acknowledgements

[1] G. F. Goya, V. Grazu, M. R. Ibarra, *Curr. Nanosci.* **2008**, *4*, 1–16.
[2] V. Hencl, P. Mucha, A. Orlikova, D. Leskova, *Water Res.* **1995**, *29*, 383–385.
[3] K. M. Krishnan, *IEEE Trans. Magnet.* **2010**, *46*, 2523–2558.

www.MaterialsViews.com

ADVANCED
FUNCTIONAL
MATERIALS
www.afm-journal.de

FULL PAPER

[4] H. Zeng, C. T. Black, R. L. Sandstrom, P. M. Rice, C. B. Murray, S. H. Sun, *Phys. Rev. B* **2006**, *73*, 4.

[5] J. M. Byrne, V. S. Coker, S. Moise, P. L. Wincott, D. J. Vaughan, F. Tuna, E. Arenholz, G. van der Laan, R. A. D. Pattrick, J. R. Lloyd, N. D. Telling, *J. R. Soc. Interface* **2013**, *10*, 20130134.

[6] L. Neel, *Annals Phys.* **1948**, *3*, 137–198.

[7] Y. Yafet, C. Kittel, *Phys. Rev.* **1952**, *87*, 290–294.

[8] R. A. D. Pattrick, G. van der Laan, C. M. B. Henderson, P. Kuiper, E. Dudzik, D. J. Vaughan, *Eur. J. Mineral.* **2002**, *14*, 1095–1102.

[9] E. J. W. Verwey, E. L. Heilmann, *J. Chem. Phys.* **1947**, *15*, 174–180.

[10] A. H. Moorish, *The Physical Principles of Magnetism*, Wiley-IEEE Press, New York, **2001**.

[11] J. M. Byrne, N. D. Telling, V. S. Coker, R. A. D. Pattrick, G. van der Laan, E. Arenholz, F. Tuna, J. R. Lloyd, *Nanotechnology* **2011**, *22*, 455709.

[12] C. M. Hansel, S. G. Benner, S. Fendorf, *Environ. Sci. Technol.* **2005**, *39*, 7147–7153.

[13] C. M. Hansel, S. G. Benner, J. Neiss, A. Dohnalkova, R. K. Kukkadapu, S. Fendorf, *Geochim. Cosmochim. Acta* **2003**, *67*, 2977–2992.

[14] V. S. Coker, N. D. Telling, G. van der Laan, R. A. D. Pattrick, C. I. Pearce, E. Arenholz, F. Tuna, R. E. P. Winpenny, J. R. Lloyd, *ACS Nano* **2009**, *3*, 1922–1928.

[15] J.-W. Moon, Y. Roh, R. J. Lauf, H. Vali, L. W. Yeary, T. J. Phelps, *J. Microbiol. Methods* **2007**, *70*, 150–158.

[16] S. Staniland, W. Williams, N. D. Telling, G. van der Laan, A. Harrison, B. Ward, *Nat. Nanotechnol.* **2008**, *3*, 158–162.

[17] L. W. Yeary, J.-W. Moon, C. J. Rawn, L. J. Love, A. J. Rondinone, J. R. Thompson, B. C. Chakoumakos, T. J. Phelps, *J. Magnet. Magnet. Mater.* **2011**, *323*, 3043–3048.

[18] V. S. Coker, J. A. Bennett, N. D. Telling, T. Henkel, J. M. Charnock, G. van der Laan, R. A. D. Pattrick, C. I. Pearce, R. S. Cutting, I. J. Shannon, J. Wood, E. Arenholz, I. C. Lyon, J. R. Lloyd, *ACS Nano* **2010**, *4*, 2577–2584.

[19] P. Kinnari, R. V. Upadhyay, R. V. Mehta, *J. Magnet. Magnet. Mater.* **2002**, *252*, 35–38.

[20] Q. Tian, Q. Wang, Q. Xie, J. Li, *Nanoscale Res. Lett.* **2010**, *5*, 1518–1523.

[21] H.-I. Hsiang, Y.-L. Liu, *J. Alloys Compd.* **2009**, *472*, 516–520.

[22] R. Shannon, *Acta Crystallogr. Section A* **1976**, *32*, 751–767.

[23] L. J. Love, L. W. Yeary, J. W. Moon, T. J. Phelps, A. J. Rondinone, *IEEE, 2005 IEEE/ASME International Conference on Advanced Intelligent Mechatronics, Vols 1 and 2* **2005**, 111–115.

[24] C. Bárcena, A. K. Sra, G. S. Chaubey, C. Khemtong, J. P. Liu, J. Gao, *Chem. Commun.* **2008**, 2224–2226.

[25] M. Drofenik, M. Kristl, D. Makovec, Z. Jagličić, D. Hanžel, *Ultrason. Sonochem.* **2008**, *15*, 791–798.

[26] D. Makovec, A. Kodre, I. Arčon, M. Drofenik, *J. Nanopart. Res.* **2011**, *13*, 1781–1790.

[27] J.-T. Jang, H. Nah, J.-H. Lee, S. H. Moon, M. G. Kim, J. Cheon, *Angew. Chem. Int. Ed.* **2009**, *48*, 1234–1238.

[28] I. S. Jacobs, *J. Appl. Phys.* **1963**, *34*, 1106–1107.

[29] A. E. Berkowitz, W. J. Schuele, P. J. Flanders, *J. Appl. Phys.* **1968**, *39*, 1261–&.

[30] V. L. Pool, M. T. Klem, J. Holroyd, T. Harris, E. Arenholz, M. Young, T. Douglas, Y. U. Idzerda, *Proc. 53rd Ann. Conf. Magnet. Magnet. Mater.* **2009**, *105*, 07B515–3.

[31] J. Takaobushi, M. Ishikawa, S. Ueda, E. Ikenaga, J.-J. Kim, M. Kobata, Y. Takeda, Y. Saitoh, M. Yabashi, Y. Nishino, D. Miwa, K. Tamasaku, T. Ishikawa, I. Satoh, H. Tanaka, K. Kobayashi, T. Kawai, *Phys. Rev. B* **2007**, *76*, 205108.

[32] W. Schiessl, W. Potzel, H. Karzel, M. Steiner, G. M. Kalvius, A. Martin, M. K. Krause, I. Halevy, J. Gal, W. Schäfer, G. Will, M. Hillberg, R. Wäppling, *Phys. Rev. B* **1996**, *53*, 9143.

[33] Y. Waseda, K. Shinoda, K. Sugiyama, *J. Phys. Sci.* **1995**, *50*, 1199–1204.

[34] S. A. Oliver, V. G. Harris, H. H. Hamdeh, J. C. Ho, *Appl. Phys. Lett.* **2000**, *76*, 2761–2763.

[35] H. Ehrhardt, S. J. Campbell, M. Hofmann, *J. Alloys Compd.* **2002**, *339*, 255–260.

[36] D. C. Dobson, J. W. Linnett, M. M. Rahman, *J. Phys. Chem. Solids* **1970**, *31*, 2727–2733.

[37] H. Tang, Y.-W. Du, Z.-Q. Qiu, J. C. Walker, *J. Appl. Phys.* **1988**, *63*, 4105–4107.

[38] R. M. Cornell, U. Schwertmann, *The iron oxides structure, properties, reactions, occurances and uses*, Wiley-VCH, Weinheim, Germany, **2003**.

[39] E. Murad, *Zeitschr. Pflanzenernahrung Bodenkunde* **1987**, *150*, 279–285.

[40] E. Murad, *Clay Minerals* **2010**, *45*, 413–430.

[41] T. Kanzaki, K. Kitayama, K. Shimokoshi, *J. Am. Ceram. Soc.* **1993**, *76*, 1491–1494.

[42] A. Kundu, C. Upadhyay, H. C. Verma, *Phys. Lett. A* **2003**, *311*, 410–415.

[43] S. J. Stewart, S. J. A. Figueroa, M. B. Sturla, R. B. Scorzelli, F. García, F. G. Requejo, *Phys. B: Condens. Matter* **2007**, *389*, 155–158.

[44] E. J. Choi, Y. Ahn, K.-C. Song, *J. Magnet. Magnet. Mater.* **2006**, *301*, 171–174.

[45] J. F. Hochepied, P. Bonville, M. P. Pileni, *J. Phys. Chem. B* **2000**, *104*, 905–912.

[46] N. Lee, T. Hyeon, *Chem. Soc. Rev.* **2012**, *41*, 2575–2589.

[47] H. Shao, C. Min, D. Issadore, M. Liong, T. J. Yoon, R. Weissleder, H. Lee, *Theranostics* **2012**, *2*, 55–65.

[48] V. Blanco-Gutierrez, M. J. Torralvo-Fernandez, R. Saez-Puche, *J. Phys. Chem. C* **2010**, *114*, 1789–1795.

[49] L. L. Stookey, *Anal. Chem.* **1970**, *42*, 779-&.

[50] J. R. Lloyd, C. Leang, A. L. H. Myerson, M. V. Coppi, S. Cuifo, B. Methe, S. J. Sandler, D. R. Lovley, *Biochem. J.* **2003**, *369*, 153–161.

[51] G. v. d. Laan, *J. Phys.: Conf. Series* **2013**, *430*, 012127.

[52] G. van der Laan, I. W. Kirkman, *J. Phys.: Condens. Matter* **1992**, *4*, 4189–4204.

[53] G. van der laan, B. T. Thole, *Phys. Rev. B* **1991**, *43*, 13401–13411.

[54] A. L. Patterson, *Phys. Rev.* **1939**, *56*, 978.

[55] P. Scherrer, *Nachr. Ges. Wiss. Goettingen* **1918**, 96–100.

[56] S. Campelj, D. Makovec, M. Drofenik, *J. Phys.: Condens. Matter* **2008**, *20*, 204101.